coatings

MDPI

Article

A Neural-Assisted Triangulation Framework for Broadband Optical Monitoring of Multilayer Coatings

Yiming Guo [1,*], Xiaohan Ji [1], Ming Ji [2,3], Yuhui Pei [1,3], Bo Wang [3] and Zhuangzhuang He [3]

[1] School of Robotics and Embodied Intelligence, Chang'an University, Xi'an 710064, China; 2024905146@chd.edu.cn (X.J.); yuhui.pei@ibdtec.cn (Y.P.)
[2] Faculty of Innovation Engineering, Macau University of Science and Technology, Taipa, Macau SAR 999078, China; jiming@ibdtec.cn
[3] IBD Technology Co., Ltd., Zhongshan 528437, China; bo.wang@ibdtec.cn (B.W.); zhuangzhuang.he@ibdtec.cn (Z.H.)
* Correspondence: gym629@chd.edu.cn; Tel.: +86-1331-918-9173

Abstract

Broadband optical monitoring provides rich spectral information for the fabrication of multilayer optical coatings, but conventional online characterization generally relies on iterative thickness re-estimation, whose computational burden increases when information from multiple deposition stages is incorporated. To address this issue, this work proposes a neural-assisted triangulation framework that organizes multistage residual spectra within a fixed-length historical observation window, thereby maintaining a fixed-dimensional estimator input. The framework further reformulates conventional iterative online thickness re-estimation as direct neural prediction of incremental thickness-state corrections. A shared one-dimensional convolutional encoder extracts spectral features from the residual history, which are then fused with the current pre-update thickness state for thickness-state updating. The updated thickness estimates are subsequently used to reconstruct the multilayer optical model and calculate the reference spectrum for the next deposition stage. The estimator is trained offline using synthetic thickness-state perturbations and a physics-guided objective that combines direct state supervision with spectral-reconstruction and spectral-gradient constraints, while only neural inference is required during online deposition. The proposed framework was implemented on an ion-beam sputtering platform and evaluated through three consecutive fabrication runs of an 82-layer long-wave-pass filter. All three fabricated filters satisfied the specified spectral requirements, with average stopband transmittance ranging from 0.090% to 0.155% and average passband transmittance ranging from 95.008% to 95.105%. The mean cutoff wavelength was 712.461 nm, with a standard deviation of 0.278 nm and a maximum inter-run difference of 0.555 nm. These results demonstrate the practical feasibility of the proposed framework for broadband monitoring of high-layer-count optical coatings.

Keywords: broadband optical monitoring; neural-assisted triangulation; historical observation window; thickness-state estimation; multilayer optical coatings; ion-beam sputtering

Check for updates

Academic Editor: Andrey V. Osipov

Received: 29 September 2026
Revised: 20 October 2026
Accepted: 24 October 2026
Published: 26 October 2026

Copyright: © 2026 by the authors. Licensee MDPI, Basel, Switzerland. This article is an open access article distributed under the terms and conditions of the Creative Commons Attribution (CC BY) license.

1. Introduction

Broadband optical monitoring (BBOM) is an important technique for controlling layer growth in multilayer optical coatings, particularly for high-layer-count interference filters whose final spectral performance is sensitive to small thickness deviations accumulated

during deposition. By acquiring spectrally resolved transmittance or reflectance measurements, BBOM provides substantially richer information than monitoring based on a single optical quantity and can support both layer termination and in situ characterization of the growing coating [1–4]. A central challenge is therefore to determine the state of the deposited multilayer structure from the measured spectra, which can be formulated as an inverse identification problem in which one or more layer thicknesses are reconstructed from the optical response [5]. In conventional sequential characterization, only the most recently deposited layer is estimated while previous thickness estimates are retained. Triangular characterization instead uses spectra acquired at different deposition stages to re-estimate multiple previously deposited layers, thereby exploiting more of the information accumulated during coating production [6]. Numerical studies have further shown that re-defining the set of already-deposited layer thicknesses can improve broadband-monitoring accuracy [7].

The use of additional historical information can improve multilayer-state estimation, but it also increases the complexity of the online inverse problem. To reduce this burden, Tikhonravov et al. proposed a modified triangular algorithm in which only selected previously deposited layers are re-estimated, retaining accuracy close to that of the full triangular approach while reducing the computational effort [8]. Related studies have shown that the choice of reconstructed layers affects both thickness-estimation accuracy and error accumulation [9], while more recent comparisons of thickness-fitting strategies have emphasized the trade-off between improved termination prediction and the computational cost of repeated fitting [10]. Historical information is also relevant because thickness errors generated during optical monitoring are not necessarily independent. Direct broadband monitoring can produce correlated errors and associated self-compensation effects, so the final spectral performance depends not only on individual layer errors but also on how these errors interact across successive deposition stages [11–13]. In addition, Sharov et al. introduced a non-local broadband monitoring algorithm that uses multiple spectral measurements acquired during layer deposition and showed numerically that additional monitoring information can reduce thickness errors [14]. These studies collectively indicate that spectral history contains useful information for coating-state reconstruction, while motivating more efficient ways to exploit such information during online production.

Learning-based inverse models provide a possible route for reducing the dependence on repeated numerical optimization, although most existing studies have focused on design or offline reconstruction rather than recursive online state estimation. Neural models have been applied to multilayer thin-film inverse design using convolutional neural networks, differentiable neural-network-like optical models, conditional invertible networks, gradient-based backpropagation, and Transformer-based generative architectures [15–20]. More directly related to fabrication-error reconstruction, Dai et al. applied a Transformer model to optical-coating manufacturing-error inversion and reported rapid inference after offline training [21]. These studies demonstrate the potential of learned or differentiable models for accelerating thin-film inverse problems, but they generally address inverse design, post-fabrication reconstruction, or offline error inversion rather than multistage state updating from broadband spectra acquired during ongoing deposition. In our previous work, a broadband optical monitoring framework with an improved error-compensation mechanism was developed for automatic coating production [22]. After each deposited layer, optical-model parameters and layer thickness were updated through a constrained random-search procedure, but the online correction still relied on iterative forward-model evaluations and was primarily driven by the terminal spectrum of the latest deposition stage. This motivates an online framework that can retain information from several re-

cent broadband observations without introducing an expanding or repeatedly solved optimization problem.

To address this need, this paper proposes a neural-assisted triangulation framework for broadband optical monitoring of multilayer coatings. The established triangulation principle is retained, while the online thickness-reestimation step is reformulated as direct neural prediction of incremental thickness-state corrections. After completion of the Nth layer, residual spectra from a fixed number of recent deposition stages are assembled into a historical observation window, and a shared one-dimensional convolutional encoder extracts spectral features from each residual observation. These historical spectral features are fused with the current pre-update thickness state and mapped to bounded incremental state corrections. The updated thickness estimates are then used to reconstruct the multilayer optical model and calculate the reference spectrum for the next deposition stage. The estimator is trained offline using synthetic thickness-state perturbations and a physics-guided objective that combines direct state supervision with spectral-reconstruction and spectral-gradient constraints. Because the observation window has a fixed length, the neural estimator maintains a fixed-dimensional input representation as the total number of deposited layers increases. The main contributions of this study are summarized as follows:

1. A fixed-dimensional historical residual representation is developed for triangulation-based broadband optical monitoring. Residual spectra from multiple recent deposition stages are organized within a moving observation window, enabling multistage spectral information to be utilized while keeping the estimator input dimension independent of the total number of deposited layers.
2. A neural-assisted multilayer state estimator is developed to reformulate iterative online thickness re-estimation as direct prediction of incremental thickness-state corrections. A shared one-dimensional convolutional encoder, masked historical feature fusion, and bounded state correction are integrated with a physics-guided training objective that constrains the predicted state through the corresponding broadband optical response.
3. The proposed framework is implemented on an ion-beam sputtering coating platform and evaluated through three consecutive fabrication runs of an 82-layer long-wave-pass filter. All three fabricated coatings satisfy the specified stopband and passband requirements, while the cutoff wavelength shows limited run-to-run variation across the three coating runs.

The remainder of this paper is organized as follows. Section 2 presents the proposed history-assisted broadband monitoring framework, including the multilayer optical model, historical state construction, neural multilayer state estimator, physics-guided training procedure, and online update strategy. Section 3 describes the experimental validation on the ion-beam sputtering platform and presents the fabrication results of the 82-layer long-wave-pass filter. Finally, Section 4 summarizes the main conclusions of this work.

2. History-Assisted Broadband Monitoring Framework

The overall architecture of the proposed neural-assisted triangulation broadband optical monitoring framework is illustrated in Figure 1. During online deposition, the terminal spectrum obtained after each completed layer is incorporated into a moving historical observation window. The corresponding residual matrix $\mathbf{E}_N$ and validity mask $\mathbf{v}_N$ are then constructed and, together with the pre-update thickness state $\hat{\mathbf{x}}_N^-$, supplied to the neural-assisted triangulation estimator F_ω. The estimator predicts an incremental thickness-state correction, which is used to update the current multilayer state. The updated thickness estimates are subsequently used to reconstruct the optical model $\mathbf{M}^{(N)}(\lambda)$ and calculate the reference transmittance spectrum for monitoring layer $N+1$. The estimator parame-

ters ω are obtained offline through physics-guided training using synthetic residual-state samples generated from thickness perturbation simulations and the thin-film forward model. Specifically, the predicted thickness-state corrections are first used to update the thickness state, after which the corresponding broadband optical response is reconstructed through the thin-film forward model. The training is then constrained by the spectral-reconstruction and spectral-gradient losses together with direct state supervision. This formulation follows the general concept of incorporating physical models and constraints into data-driven learning [23]. Related studies include physics-guided neural-network modeling and neural-network-based multilayer optical inverse-design approaches [24,25].

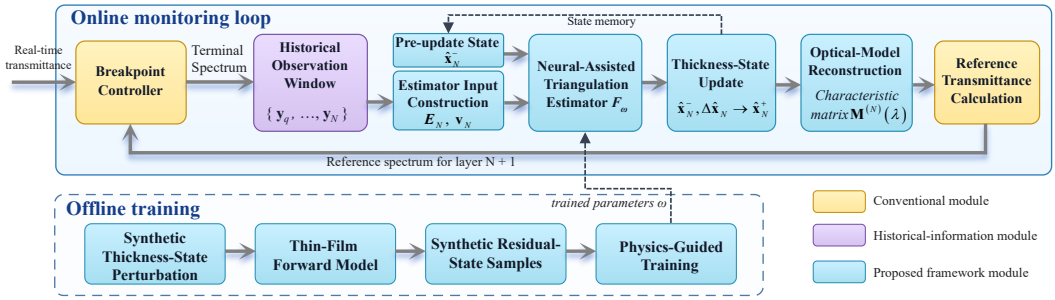


Figure 1. Overall architecture of the proposed neural-assisted triangulation broadband monitoring framework.

2.1. Multilayer Optical Forward Model

For a multilayer stack containing j deposited layers, the broadband transmittance is calculated using the characteristic-matrix formulation of thin-film optics under normal incidence. For the ith layer, the characteristic matrix at wavelength λ is written as

$$\mathbf{M}_i(\lambda) = \begin{bmatrix} \cos\delta_i & \frac{\mathrm{i}\sin\delta_i}{\eta_i} \\ \mathrm{i}\eta_i\sin\delta_i & \cos\delta_i \end{bmatrix}, \qquad \delta_i = \frac{2\pi n_i d_i}{\lambda}, \tag{1}$$

where n_i, η_i, and d_i denote the refractive index, optical admittance, and physical thickness of the ith layer, respectively. Under normal incidence for nonmagnetic materials, $\eta_i = n_i$. The characteristic matrix of the deposited multilayer stack is obtained as

$$\mathbf{M}^{(j)}(\lambda) = \prod_{i=1}^{j} \mathbf{M}_i(\lambda), \tag{2}$$

where the matrix product follows the physical order of the deposited layers.

Using the multilayer characteristic matrix together with the optical admittances of the incident medium and substrate, the broadband transmittance spectrum after deposition of the jth layer is represented compactly by

$$\mathcal{T}_j(d_1, d_2, \ldots, d_j) = \left[T_j^{\mathrm{mod}}(\lambda_1; d_1, \ldots, d_j), \ldots, T_j^{\mathrm{mod}}(\lambda_m; d_1, \ldots, d_j)\right]^{\mathrm{T}}, \tag{3}$$

where $T_j^{\mathrm{mod}}(\lambda_l; d_1, \ldots, d_j)$ denotes the modeled transmittance at wavelength λ_l, with $l = 1, \ldots, m$. Here, $\mathcal{T}_j(\cdot)$ represents the thin-film forward model, in which the calibrated optical constants are fixed and only the layer thicknesses are treated as variable inputs.

2.2. History-Based Triangulation State Construction

During multilayer deposition, the spectrum measured after each layer contains the accumulated optical response of all previously deposited layers. Therefore, spectra acquired at different deposition stages provide partially overlapping constraints on the thicknesses

of the deposited layers. In this study, these successive observations are jointly utilized to estimate the thickness-state corrections of multiple recent layers, providing the measurement basis for the neural-assisted triangulation estimator developed below.

Let

$$\mathbf{y}_j = \left[T_j^{\text{meas}}(\lambda_1), T_j^{\text{meas}}(\lambda_2), \ldots, T_j^{\text{meas}}(\lambda_m)\right]^{\mathrm{T}} \tag{4}$$

denote the broadband transmittance spectrum of the deposited multilayer stack measured after termination of the jth layer, where m is the number of wavelength samples. After completion of the Nth layer, a moving historical observation window is constructed as

$$\mathcal{H}_N = \{\mathbf{y}_q, \mathbf{y}_{q+1}, \ldots, \mathbf{y}_N\}, \qquad q = \max(1, N - K + 1), \tag{5}$$

where K is the prescribed triangulation window length and q denotes the first valid deposition-stage index in the current observation window. Thus, each state update uses at most the K most recent terminal spectra. The thickness estimates of layers preceding the current window are retained at their latest values and are not re-estimated during the current update.

For each spectrum in $\mathcal{H}_N$, the corresponding pre-update modeled spectrum is calculated from the current thickness estimates through the forward model as

$$\hat{\mathbf{y}}_j^- = \mathcal{T}_j\left(\hat{d}_1^-, \hat{d}_2^-, \ldots, \hat{d}_j^-\right), \tag{6}$$

where $\hat{d}_i^-$ denotes the latest estimate of the ith-layer thickness immediately before the current state update. The corresponding spectral residual is then defined as

$$\mathbf{e}_j = \mathbf{y}_j - \hat{\mathbf{y}}_j^-. \tag{7}$$

Because the spectrum measured after the jth layer depends on the optical response of all layers deposited up to that stage, successive residual spectra provide partially overlapping information for updating the thickness states of the layers within the current observation window. Joint use of these residuals therefore enables multiple layer states to be updated simultaneously rather than correcting only the most recently deposited layer.

To maintain a fixed input dimension for the neural estimator, the residual spectra are arranged according to their deposition order as

$$\mathbf{E}_N = \begin{bmatrix} \mathbf{e}_{N-K+1}^{\mathrm{T}} \\ \mathbf{e}_{N-K+2}^{\mathrm{T}} \\ \vdots \\ \mathbf{e}_N^{\mathrm{T}} \end{bmatrix} \in \mathbb{R}^{K \times m}. \tag{8}$$

A binary validity mask is defined as

$$\mathbf{v}_N = [v_{N-K+1}, v_{N-K+2}, \ldots, v_N]^{\mathrm{T}} \in \{0,1\}^K, \tag{9}$$

where $v_j = 1$ for valid deposition stages ($j \geq 1$) and $v_j = 0$ otherwise. For notational convenience, residual and state entries associated with unavailable deposition stages ($j < 1$) are understood to be zero-padded throughout. Once the observation window is fully populated, it moves forward with the deposition process and retains only the K most recent residual spectra.

The residual matrix $\mathbf{E}_N$ and validity mask $\mathbf{v}_N$ provide the fixed-dimensional historical input to the neural estimator. They are subsequently combined with the pre-update

thickness-state vector $\hat{\mathbf{x}}_N^-$ defined in the following subsection. Since K is fixed, the estimator input dimensions remain independent of the total number of deposited layers.

Remark 1. *Triangular algorithms have previously been used in broadband optical monitoring to exploit measurement spectra acquired at multiple deposition stages for re-estimating deposited-layer thicknesses [6]. Subsequent variants reduce the number of thickness variables involved in the online optimization, including modified and hybrid triangular strategies that restrict the set of re-estimated layers [8,10]. The present framework follows the same multi-stage characterization principle but reformulates the online estimation step as direct neural prediction of incremental thickness-state corrections from a fixed-dimensional residual-state representation.*

2.3. Neural Multilayer State Estimator

The layer-dependent state considered in this study is the relative deviation of the deposited thickness from its design value. Since the actual deposited thickness is not directly available during online monitoring, this state is represented by its current estimate. Thickness deviations modify the accumulated optical phase and consequently affect the broadband spectra measured at subsequent deposition stages.

The normalized pre-update thickness state of the jth layer is defined as

$$\hat{x}_j^- = \frac{\hat{d}_j^- - d_j^{\mathrm{des}}}{d_j^{\mathrm{des}}}, \tag{10}$$

where d_j^{des} denotes the design thickness of the jth layer. Thus, $\hat{x}_j^-$ represents the dimensionless relative deviation of the current thickness estimate from the design value.

The pre-update state vector corresponding to the current observation window is constructed in the same window order as

$$\hat{\mathbf{x}}_N^- = \left[\hat{x}_{N-K+1}^-, \hat{x}_{N-K+2}^-, \ldots, \hat{x}_N^-\right]^{\mathrm{T}} \in \mathbb{R}^K. \tag{11}$$

The ordering of $\hat{\mathbf{x}}_N^-$ is aligned with that of the residual matrix $\mathbf{E}_N$ and the validity mask $\mathbf{v}_N$, such that each valid state component corresponds to the residual spectrum acquired at the same deposition stage, while unavailable positions are zero-padded.

Rather than directly predicting the absolute layer thicknesses, the proposed estimator predicts an incremental correction conditioned on the spectral residual history and the current normalized thickness state,

$$\Delta\hat{\mathbf{x}}_N = F_{\boldsymbol{\omega}}\left(\mathbf{E}_N, \mathbf{v}_N, \hat{\mathbf{x}}_N^-\right) \in \mathbb{R}^K, \tag{12}$$

where $F_{\boldsymbol{\omega}}(\cdot)$ denotes the neural estimator with trainable parameters $\boldsymbol{\omega}$. The inclusion of $\hat{\mathbf{x}}_N^-$ provides the estimator with the current pre-update thickness state, while $\mathbf{E}_N$ characterizes the spectral mismatch associated with the current model estimates. The components of $\Delta\hat{\mathbf{x}}_N$ follow the same window ordering as $\hat{\mathbf{x}}_N^-$ and $\mathbf{v}_N$, and correspond to the rows of $\mathbf{E}_N$ associated with the same deposition stages.

The state is subsequently updated according to

$$\hat{\mathbf{x}}_N^+ = \mathrm{clip}\left(\hat{\mathbf{x}}_N^- + \mathbf{v}_N \odot \Delta\hat{\mathbf{x}}_N, -c_d, c_d\right), \tag{13}$$

where $\odot$ denotes element-wise multiplication and $\mathrm{clip}(\mathbf{z}, -c_d, c_d)$ limits each element of $\mathbf{z}$ to the interval $[-c_d, c_d]$. The parameter $c_d > 0$ therefore specifies the admissible range of the normalized thickness state, such that $-c_d \le \hat{x}_j^+ \le c_d$.

For each valid layer within the current observation window, the updated thickness estimate is recovered from the normalized state as

$$\hat{d}_j^{+} = d_j^{\mathrm{des}}\left(1 + \hat{x}_j^{+}\right), \tag{14}$$

where $\hat{x}_j^{+}$ denotes the component of $\hat{\mathbf{x}}_N^{+}$ associated with the jth layer. The thickness estimates of previously deposited layers preceding the current observation window retain their latest values. Thus, the estimator performs residual-guided incremental refinement of the current thickness-state estimates.

2.3.1. Spectral Feature Extraction and Fusion

The architecture of the proposed neural-assisted triangulation estimator is illustrated in Figure 2. For clarity, in Figure 2, 1D-CNN denotes a one-dimensional convolutional neural network, FC denotes a fully connected layer, and ReLU denotes the rectified linear unit activation function. The estimator combines residual-spectrum features extracted from the historical observation window with the current pre-update thickness state to predict an incremental thickness-state correction.

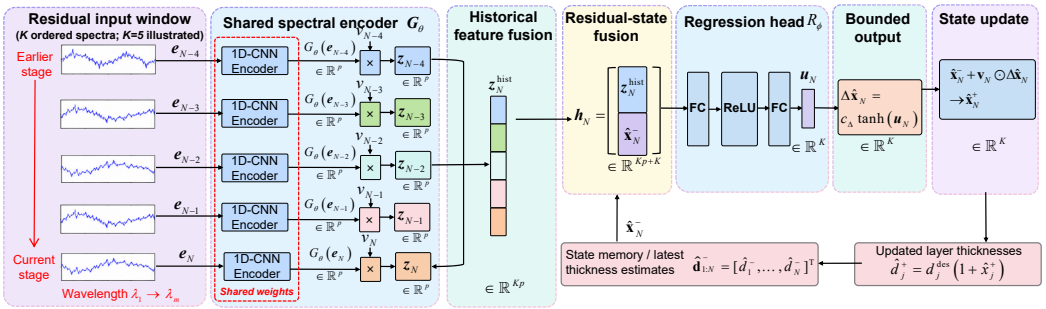


Figure 2. Architecture of the proposed neural-assisted triangulation estimator. The residual input window contains K ordered residual spectra sampled along wavelength; $K = 5$ is illustrated here. Each residual spectrum e_j is encoded by the shared spectral encoder G_θ, and the resulting feature $G_\theta(e_j)$ is multiplied by the corresponding validity mask v_j to obtain z_j before historical feature fusion.

Each residual spectrum in the observation window is treated as a one-dimensional sequence sampled along wavelength. A shared one-dimensional convolutional encoder $G_{\boldsymbol{\theta}} : \mathbb{R}^m \rightarrow \mathbb{R}^p$ maps each residual spectrum to a p-dimensional learned spectral representation,

$$\mathbf{z}_j = v_j G_{\boldsymbol{\theta}}(\mathbf{e}_j) \in \mathbb{R}^p, \qquad j = N - K + 1, \ldots, N, \tag{15}$$

where $\boldsymbol{\theta}$ denotes the trainable parameters of the shared spectral encoder. Multiplication by v_j suppresses the encoded features associated with padded positions. The resulting spectral features are assembled in deposition order to form the historical representation

$$\mathbf{z}_N^{\mathrm{hist}} = \left[\mathbf{z}_{N-K+1}^{\mathrm{T}}, \mathbf{z}_{N-K+2}^{\mathrm{T}}, \ldots, \mathbf{z}_N^{\mathrm{T}}\right]^{\mathrm{T}} \in \mathbb{R}^{Kp}. \tag{16}$$

To account for the current thickness state, this historical representation is combined with the pre-update thickness-state vector to form

$$\mathbf{h}_N = \begin{bmatrix} \mathbf{z}_N^{\mathrm{hist}} \\ \hat{\mathbf{x}}_N^{-} \end{bmatrix} \in \mathbb{R}^{Kp+K}, \tag{17}$$

where $\mathbf{h}_N$ denotes the joint residual-state representation supplied to the regression head.

A fully connected regression head maps $\mathbf{h}_N$ to an unconstrained raw correction vector,

$$\mathbf{u}_N = R_{\boldsymbol{\phi}}(\mathbf{h}_N) \in \mathbb{R}^K, \tag{18}$$

where $R_{\boldsymbol{\phi}}(\cdot)$ denotes the regression head parameterized by the trainable parameters $\boldsymbol{\phi}$. The incremental thickness-state correction is then obtained through an element-wise bounded activation,

$$\Delta\hat{\mathbf{x}}_N = c_\Delta \tanh(\mathbf{u}_N), \tag{19}$$

where $c_\Delta > 0$ bounds the magnitude of the normalized correction produced in a single state update. The complete trainable parameter set is $\boldsymbol{\omega} = \{\boldsymbol{\theta}, \boldsymbol{\phi}\}$.

Since the observation-window length K, the wavelength sampling grid, and the encoded feature dimension p are fixed, the architecture and computational cost of the neural estimator remain independent of the total number of deposited layers.

2.3.2. Synthetic Training Sample Generation

The neural estimator is trained offline using synthetic multilayer deposition samples generated from controlled thickness perturbations and the thin-film forward model. For each synthetic sample, the deposited thickness of the ith layer is generated by perturbing the corresponding design thickness,

$$d_i^{\mathrm{syn}} = d_i^{\mathrm{des}}(1 + \xi_i), \qquad \xi_i \sim \mathcal{D}_d, \tag{20}$$

where d_i^{syn} denotes the synthetically generated thickness of the ith layer, ξ_i is the normalized deposition-thickness perturbation, and $\mathcal{D}_d$ denotes its prescribed distribution.

To emulate the pre-update thickness estimates encountered during online estimation, a synthetic realization of $\hat{d}_i^-$ is generated relative to d_i^{syn} as

$$\hat{d}_i^- = d_i^{\mathrm{syn}} - d_i^{\mathrm{des}}\delta_i, \qquad \delta_i \sim \mathcal{D}_p, \tag{21}$$

where δ_i denotes the normalized deviation of the pre-update estimate from the corresponding synthetic thickness, and $\mathcal{D}_p$ denotes its prescribed distribution. This construction provides synthetic realizations of the same pre-update quantity used during online estimation, rather than reproducing the recursive estimation history explicitly.

The target incremental thickness-state correction is therefore known directly as

$$\Delta x_i^{\mathrm{tar}} = \frac{d_i^{\mathrm{syn}} - \hat{d}_i^-}{d_i^{\mathrm{des}}} = \delta_i. \tag{22}$$

The distributions $\mathcal{D}_d$ and $\mathcal{D}_p$ are bounded and zero-centered, with their ranges selected to represent the expected fabrication and pre-update estimation deviations. The generated samples are restricted to satisfy $|\xi_i| \le c_d$, $|\xi_i - \delta_i| \le c_d$, and $|\delta_i| \le c_\Delta$.

For each simulated deposition stage j, the synthetic observation spectrum is generated from the corresponding synthetic thicknesses using the thin-film forward model,

$$\mathbf{y}_j^{\mathrm{syn}} = \mathcal{T}_j\left(d_1^{\mathrm{syn}}, d_2^{\mathrm{syn}}, \ldots, d_j^{\mathrm{syn}}\right) \in \mathbb{R}^m. \tag{23}$$

Here, $\mathbf{y}_j^{\mathrm{syn}}$ is the synthetic counterpart of the measured spectrum $\mathbf{y}_j$ used during online deposition. Using the corresponding synthetic pre-update thickness estimates, the modeled spectrum $\hat{\mathbf{y}}_j^-$ is calculated according to Equation (6). The synthetic residual spectrum is then defined as

$$\mathbf{e}_j^{\mathrm{syn}} = \mathbf{y}_j^{\mathrm{syn}} - \hat{\mathbf{y}}_j^-. \tag{24}$$

For a training sample corresponding to deposition stage N, the valid synthetic residual spectra are those associated with stages $j = q, \ldots, N$, where q is defined in Equation (5). The residual matrix $\mathbf{E}_N^{\mathrm{syn}}$ is assembled from $\mathbf{e}_j^{\mathrm{syn}}$, $j = q, \ldots, N$, using the same ordering and zero-padding strategy as the online residual matrix $\mathbf{E}_N$. The validity mask $\mathbf{v}_N$ and the pre-update thickness-state vector $\hat{\mathbf{x}}_N^-$ are constructed using the same window representation as in online estimation.

The target correction vector $\Delta\mathbf{x}_N^{\mathrm{tar}} \in \mathbb{R}^K$ is assembled using the same window ordering, with entries corresponding to unavailable deposition stages ($j < 1$) set to zero. Thus, each synthetic training sample consists of the estimator input $\left(\mathbf{E}_N^{\mathrm{syn}}, \mathbf{v}_N, \hat{\mathbf{x}}_N^-\right)$, the corresponding target correction $\Delta\mathbf{x}_N^{\mathrm{tar}}$, and the synthetic spectra $\mathbf{y}_j^{\mathrm{syn}}$ required for the physics-guided spectral losses. Samples with $N < K$ are retained so that the estimator is also trained under the zero-padded conditions encountered during the initial deposition stages.

2.3.3. Physics-Guided Training Objective

The training objective combines direct supervision in the thickness-state space with physics-based consistency constraints in the spectral domain. The supervised state loss is defined as

$$L_{\mathrm{state}} = \frac{\left\| \mathbf{v}_N \odot \left(\Delta\hat{\mathbf{x}}_N - \Delta\mathbf{x}_N^{\mathrm{tar}} \right) \right\|_1}{\|\mathbf{v}_N\|_1}, \tag{25}$$

where the validity mask excludes padded positions from the state supervision.

For the current observation window, the post-update thickness state $\hat{\mathbf{x}}_N^+$ is obtained from Equation (13). For layers within the current window, the corresponding post-update physical thicknesses are obtained from the thickness-state relation defined above. Layers preceding the current window retain their latest estimates, such that $\hat{d}_i^+ = \hat{d}_i^-$ for $i < q$.

For each valid deposition stage, the corresponding post-update modeled spectrum is reconstructed as

$$\hat{\mathbf{y}}_j^+ = \mathcal{T}_j\left(\hat{d}_1^+, \hat{d}_2^+, \ldots, \hat{d}_j^+\right), \qquad j = q, \ldots, N. \tag{26}$$

Let $K_N = N - q + 1 = \|\mathbf{v}_N\|_1$ denote the number of valid deposition stages in the current observation window. The spectral reconstruction loss is then defined as

$$L_{\mathrm{rec}} = \frac{1}{K_N m} \sum_{j=q}^{N} \left\| \mathbf{y}_j^{\mathrm{syn}} - \hat{\mathbf{y}}_j^+ \right\|_1. \tag{27}$$

This term constrains the predicted thickness correction according to the broadband optical response produced by the multilayer forward model.

To additionally account for local spectral variation, a discrete wavelength-difference operator $\mathbf{D}_\lambda : \mathbb{R}^m \to \mathbb{R}^{m-1}$ is defined for an arbitrary spectrum $\mathbf{a} = [a_1, \ldots, a_m]^{\mathrm{T}}$ as

$$[\mathbf{D}_\lambda \mathbf{a}]_r = \frac{a_{r+1} - a_r}{\lambda_{r+1} - \lambda_r}, \qquad r = 1, \ldots, m-1. \tag{28}$$

The spectral-gradient loss is defined as

$$L_{\mathrm{grad}} = \frac{1}{K_N(m-1)} \sum_{j=q}^{N} \left\| \mathbf{D}_\lambda \mathbf{y}_j^{\mathrm{syn}} - \mathbf{D}_\lambda \hat{\mathbf{y}}_j^+ \right\|_1. \tag{29}$$

The overall training objective is

$$L = \alpha L_{\mathrm{state}} + \beta L_{\mathrm{rec}} + \gamma L_{\mathrm{grad}}, \tag{30}$$

where α, β, and γ are weighting coefficients used to balance the numerical scales and relative contributions of the three loss terms. The three loss terms impose complementary constraints: L_{state} directly supervises the normalized thickness-state correction, whereas L_{rec} and L_{grad} constrain the corresponding optical response in terms of spectral magnitude and local spectral variation, respectively.

Remark 2. *During online monitoring, the updated thickness estimates obtained after deposition stage N are used to reconstruct the optical model and calculate the reference transmittance spectrum for the next layer. For $N < N_{\text{total}}$,*

$$\mathbf{y}_{N+1}^{\text{ref}} = \mathcal{T}_{N+1}\left(\hat{d}_1^{+}, \ldots, \hat{d}_N^{+}, d_{N+1}^{\text{des}}\right), \tag{31}$$

where d_{N+1}^{des} is the design thickness of the next layer. The resulting reference spectrum is then used for broadband breakpoint control of layer $N+1$. The complete online update procedure is summarized in Algorithm 1.

Algorithm 1: Online neural-assisted triangulation update

Input: Design multilayer structure, trained estimator F_ω, window length K
Output: Updated multilayer thickness estimates

Initialize the thickness estimates using the design values;
Initialize the historical spectrum buffer $\mathcal{H}$;
Calculate the initial reference spectrum for layer 1;
for $N = 1$ **to** N_{total} **do**
    Deposit layer N under broadband breakpoint control;
    Acquire the terminal spectrum $\mathbf{y}_N$ and update $\mathcal{H}$;
    Determine $q = \max(1, N - K + 1)$;
    Construct $\mathbf{E}_N$, $\mathbf{v}_N$, and $\hat{\mathbf{x}}_N^-$;
    Estimate $\Delta\hat{\mathbf{x}}_N = F_\omega(\mathbf{E}_N, \mathbf{v}_N, \hat{\mathbf{x}}_N^-)$;
    Update the thickness state according to Equation (13);
    Recover and store the updated physical thickness estimates;
    Reconstruct $\mathbf{M}^{(N)}(\lambda)$ using the latest thickness estimates;
    if $N < N_{\text{total}}$ **then**
        Calculate $\mathbf{y}_{N+1}^{\text{ref}}$ for monitoring layer $N+1$;

3. Experimental Validation

To evaluate the practical performance of the proposed neural-assisted triangulation broadband monitoring method, an 82-layer long-wave-pass filter design was fabricated in three consecutive coating runs using an ion-beam sputtering coating system. The experiments were conducted directly on the production-scale ion-beam sputtering coating platform shown in Figure 3 to evaluate the practical effectiveness and run-to-run repeatability of the proposed monitoring strategy under actual deposition conditions.

3.1. Experimental Platform and Coating Task

The structure of the production-scale ion-beam sputtering coating platform used for multilayer coating fabrication is shown in Figure 3. The platform mainly consists of a vacuum chamber, an ion-beam sputtering source, an auxiliary ion source, a rotating substrate holder, and a broadband optical monitoring system. The broadband transmittance during deposition was acquired using an optical monitoring system (model: IBD-MNOMS; IBD Technology Co., Ltd., Zhongshan, China). The substrates were mounted on a rotating

holder, and the rotation speed during optical monitoring was set to 20 revolutions per minute (rpm).

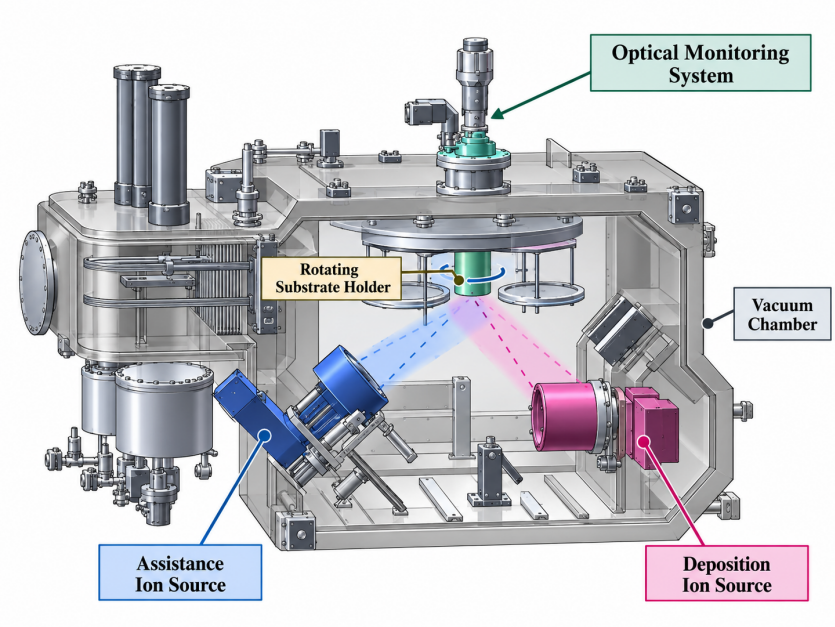


Figure 3. Structure of the production-scale ion-beam sputtering coating platform used for broadband optical monitoring and multilayer coating fabrication.

The coating stack was fabricated using Ta_2O_5 and SiO_2 as separate dielectric layer materials on a K9 glass substrate; they were not deposited as a mixed Ta_2O_5–SiO_2 nanocluster or composite layer. No dedicated crystallographic characterization was performed in this study, and therefore the crystal phase of the deposited films was not determined. The deposition process was performed at a substrate temperature of approximately 100 °C and a base pressure of approximately 2.0×10^{-4} Pa. Under the selected process conditions, the nominal deposition rates of Ta_2O_5 and SiO_2 were approximately 1.987 Å/s and 1.527 Å/s, respectively.

In the present multilayer coating, Ta_2O_5 is used as a transition-metal-oxide dielectric layer rather than as a metallic transition-metal layer. Its primary optical role is to provide refractive-index contrast with SiO_2, thereby contributing to the optical phase accumulation and interference behavior of the multilayer stack. Variations in composition, stoichiometry, or oxidation state may affect the complex refractive index and optical absorption of transition-metal oxides; these effects were not separately characterized in the present study.

3.2. Spectral Performance of the 82-Layer Filter

The test coating was an 82-layer long-wave-pass filter designed for the spectral range of 400–1200 nm. The specified optical performance required an average transmittance below 0.5% in the 400–700 nm stopband and an average transmittance above 95% in the 715–1200 nm passband.

During each coating run, the proposed neural-assisted triangulation monitoring framework was executed online throughout the multilayer deposition process. After termination of each layer, the newly acquired broadband spectrum was incorporated into the fixed observation window, and the trained neural estimator was used to update the thickness states of the corresponding layers. The reconstructed multilayer state was subsequently used to calculate the reference spectrum for the next deposition stage. The neural es-

timator was trained offline, and only forward inference was performed during online coating production.

The triangulation window length was set to $K = 5$. The maximum normalized correction allowed in a single state update was set to $c_\Delta = 0.05$, while the admissible relative thickness-state range was set to $c_d = 0.10$. Consequently, the thickness correction predicted in each update was limited to ±5% of the corresponding design thickness, and the updated thickness state was constrained within ±10% of the design value. These bounds limit excessively large state corrections while preserving a practical correction range for online thickness-state updating.

Three consecutive coating runs were performed using the same film design and nominal process conditions. Figure 4 compares the measured transmittance spectrum of each coating run with the design reference spectrum. Panels (a)–(c) of Figure 4 correspond to Run 1, Run 2, and Run 3, respectively. All three measured spectra exhibit the expected long-wave-pass characteristics, including a low-transmittance stopband, a well-defined transition edge, and a high-transmittance passband. The spectra are displayed over an extended wavelength range to illustrate the overall spectral behavior, whereas the quantitative performance evaluation is restricted to the specified 400–1200 nm range.

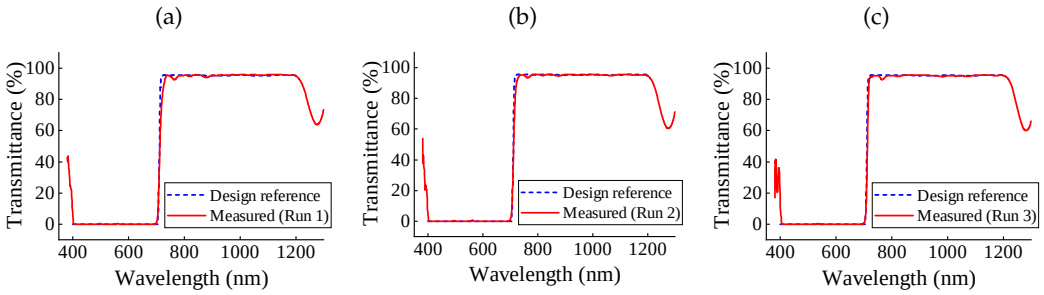


Figure 4. Comparison between the design reference spectrum and the measured transmittance spectra of the 82-layer long-wave-pass filter obtained from three consecutive coating runs: (**a**) Run 1; (**b**) Run 2; and (**c**) Run 3.

As shown in Figure 4, the measured spectra from all three coating runs closely follow the overall spectral profile of the design reference. For quantitative evaluation, the average transmittance was calculated separately over the 400–700 nm stopband and the 715–1200 nm passband. The stopband average transmittances of Runs 1–3 were 0.092%, 0.090%, and 0.155%, respectively, while the corresponding passband average transmittances were 95.059%, 95.008%, and 95.105%. Therefore, all three fabricated filters satisfied the specified requirements of $T_{\text{ave}} < 0.5\%$ in the stopband and $T_{\text{ave}} > 95\%$ in the passband. The small variation among the three runs also indicates consistent band-averaged spectral performance under repeated coating conditions.

To further evaluate the spectral-edge control performance, the transition regions of the three measured spectra are compared in Figure 5a. The cutoff wavelength λ_{50} is defined as the wavelength at which the transmittance reaches 50%. As shown by the enlarged region, the transition edges obtained from the three consecutive coating runs remain closely distributed.

The cutoff wavelengths of Runs 1–3 were 712.454, 712.187, and 712.742 nm, respectively. The mean cutoff wavelength was 712.461 nm, and the maximum difference among the three runs was only 0.555 nm. These results indicate good run-to-run stability of the spectral-edge position during the 82-layer coating process.

To further examine the deviation of the transition edge from the design reference, the wavelength-dependent transmittance deviation is defined as

$$\Delta T_r(\lambda) = T_r^{\mathrm{meas}}(\lambda) - T^{\mathrm{des}}(\lambda), \qquad r = 1, 2, 3, \tag{32}$$

where $T^{\mathrm{des}}(\lambda)$ denotes the design transmittance spectrum.

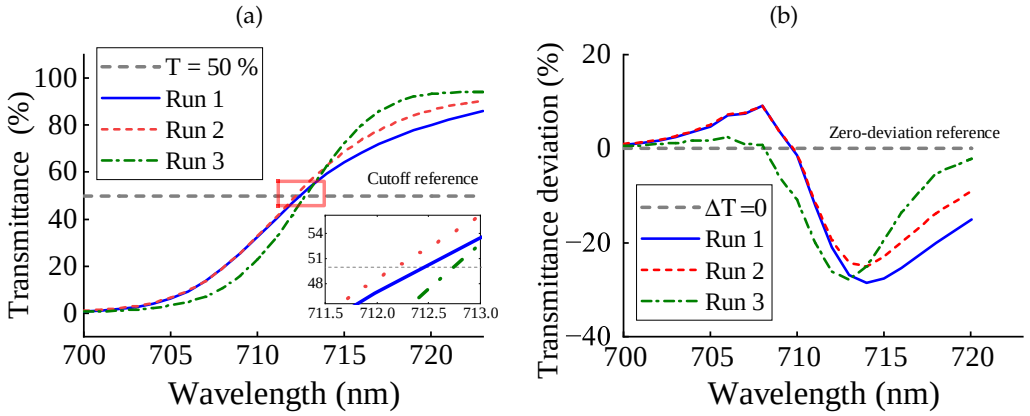


Figure 5. Spectral-edge characteristics of the 82-layer long-wave-pass filter obtained from three consecutive coating runs. The colored curves represent the three independent coating runs. (**a**) Enlarged transition regions of the measured transmittance spectra. The horizontal dashed line at $T = 50\%$ serves as the reference for identifying the cutoff wavelength λ_{50} and comparing the run-to-run consistency near the spectral edge; the inset highlights the cutoff region. (**b**) Wavelength-dependent transmittance deviations between the measured spectra and the design reference. The horizontal dashed line at $\Delta T = 0$ denotes zero transmittance deviation and provides a reference for comparing the wavelength-dependent deviations among the three coating runs.

As shown in Figure 5b, the deviations remain relatively small on the short-wavelength side of the transition region and increase substantially near the steep spectral edge. The three deviation curves exhibit similar wavelength-dependent trends, with the largest differences occurring around the region of maximum spectral slope. This behavior is expected because a small displacement of a steep transition edge can produce a comparatively large transmittance difference at the same wavelength.

The transition width is further defined as

$$W_{10-90} = \lambda_{90} - \lambda_{10}, \tag{33}$$

where λ_{10} and λ_{90} denote the wavelengths at which the measured transmittance reaches 10% and 90%, respectively.

3.3. Repeatability of Consecutive Coating Runs

The run-to-run repeatability of the proposed monitoring method was further evaluated using the three consecutive coating experiments. The mean measured transmittance spectrum is defined as

$$\bar{T}(\lambda) = \frac{1}{3}\sum_{r=1}^{3} T_r(\lambda), \tag{34}$$

and the corresponding wavelength-dependent standard deviation is calculated as

$$\sigma_T(\lambda) = \sqrt{\frac{1}{2}\sum_{r=1}^{3}[T_r(\lambda) - \bar{T}(\lambda)]^2}. \tag{35}$$

Figure 6a shows the mean transmittance spectrum of the three consecutive coating runs, with the shaded region representing one standard deviation. SD denotes standard deviation. The relatively narrow deviation band over most of the stopband and passband indicates good run-to-run consistency of the fabricated filters. Larger deviations are mainly observed in spectral regions with rapid transmittance variation, particularly near the transition edge and the long-wavelength roll-off region. Figure 6b further presents the wavelength-dependent standard deviation of the measured transmittance. The standard deviation remains small over most of the relatively flat stopband and passband regions, whereas a pronounced peak appears near the transition edge. This behavior is consistent with the increased spectral sensitivity in regions where the transmittance changes rapidly with wavelength. A relatively large variation is also observed near the short-wavelength measurement boundary below approximately 400 nm. This variation may be influenced by the lower signal level and increased measurement sensitivity near the lower spectral limit of the monitoring system.

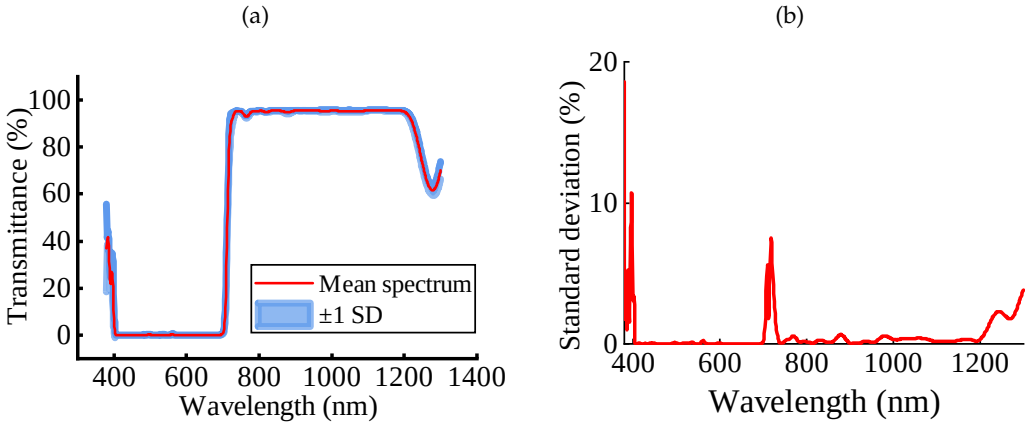


Figure 6. Run-to-run repeatability of the 82-layer long-wave-pass filter over three consecutive coating runs. (**a**) Mean measured transmittance spectrum, with the shaded region denoting one standard deviation among the three runs. (**b**) Wavelength-dependent standard deviation of the measured transmittance.

The quantitative spectral characteristics of the three consecutive coating runs are summarized in Table 1. The mean stopband transmittance was only 0.112%, while the mean passband transmittance reached 95.057%, confirming that all three fabricated filters satisfied the specified spectral requirements. In addition, the cutoff wavelength showed a mean value of 712.461 nm with a standard deviation of only 0.278 nm, indicating good run-to-run stability of the spectral-edge position.

Table 1. Spectral performance and repeatability of three consecutive coating runs.

Metric	Run 1	Run 2	Run 3	Mean ± SD
T_{ave}^{stop} (%)	0.092	0.090	0.155	0.112 ± 0.037
T_{ave}^{pass} (%)	95.059	95.008	95.105	95.057 ± 0.049
λ_{50} (nm)	712.454	712.187	712.742	712.461 ± 0.278
W_{10-90} (nm)	20.653	16.353	10.268	15.758 ± 5.218

The transition width $W_{10–90}$ exhibited a comparatively larger run-to-run variation, with values of 20.653, 16.353, and 10.268 nm for Runs 1–3, respectively, corresponding to a mean of 15.758 nm and a standard deviation of 5.218 nm. In contrast, the cutoff wavelength remained highly repeatable (712.461 ± 0.278 nm). Since a smaller $W_{10–90}$ corresponds to a steeper transition edge, these results indicate that the cutoff position remained stable,

whereas the transition-edge steepness varied more noticeably among the three coating runs. This difference can be partly understood from the constraints of the proposed monitoring framework. The neural-assisted triangulation method performs bounded thickness-state corrections based on historical spectral residuals. Although the spectral-gradient loss L_{grad} encourages local spectral-gradient consistency during offline training, the transition width is not explicitly imposed as a hard constraint. Therefore, the framework does not guarantee identical transition-edge steepness across independent fabrication runs.

Residual thickness deviations in edge-sensitive layers and small variations in the optical properties of deposited films may contribute to the observed differences. However, complete layer-resolved thickness-estimation histories were not recorded for the three fabrication runs, and independent measurements of process-induced optical-property variations were not performed. Consequently, the observed variation cannot be reliably attributed to specific layers or a single physical mechanism. Furthermore, the correction bound $c_{\Delta} = 0.05$ limits the magnitude of each normalized thickness-state update but does not directly constrain the transition width. Increasing the spectral-gradient loss weight γ may strengthen local spectral-gradient consistency, but its effect on transition-width repeatability requires dedicated sensitivity analysis.

Overall, the three consecutive coating experiments demonstrate that the proposed neural-assisted triangulation monitoring framework can achieve the specified stopband and passband transmittance requirements while maintaining high repeatability of the cutoff wavelength. The wavelength-resolved repeatability analysis further shows that spectral variation remains limited over most of the working spectral range, with larger deviations mainly concentrated in regions of rapid spectral change.

3.4. Hyperparameter Sensitivity Analysis

To investigate the influence of the historical window length and the correction bound, additional numerical sensitivity analyses were conducted using the 82-layer coating design. As shown in Table 2, the proposed configuration ($K = 5$, $c_{\Delta} = 0.05$) achieves a favorable balance between spectral reconstruction accuracy and the complexity of historical information processing.

Table 2. Sensitivity analysis of the historical window length and correction bound under relatively large initial thickness-estimation errors.

Historical Window K	Correction Bound c_{Δ}	Thickness-State MAE (%)	Spectral MAE (pp)
1	0.02	2.2342	2.7326
1	0.05	1.3234	2.5995
1	0.10	1.4896	2.6534
3	0.02	2.2281	2.6483
3	0.05	1.3199	2.4998
3	0.10	1.5008	2.5732
5	0.02	2.2233	2.5438
5	**0.05**	**1.3184**	**2.4163**
5	0.10	1.4964	2.4649
8	0.02	2.2201	2.4369
8	0.05	1.3153	2.3156
8	0.10	1.4896	2.3795

Note: All results correspond to the same held-out test conditions with initial normalized thickness-estimation errors $|\delta| \leq 0.06$. Thickness-state MAE represents the current-layer normalized thickness estimation error, and spectral MAE represents the post-update spectral reconstruction error in transmittance percentage points (pp). Bold values indicate the adopted parameter configuration.

The historical window length and single-step correction bound were systematically evaluated using 12 parameter combinations, with $K = 1, 3, 5, 8$ and $c_{\Delta} = 0.02, 0.05, 0.10$,

while $c_d = 0.10$ was kept constant. As shown in Table 2, increasing the historical window length generally improved spectral reconstruction accuracy under relatively large initial thickness-estimation errors. For $c_\Delta = 0.05$, the post-update spectral MAEs decreased from 2.5995 to 2.4998, 2.4163, and 2.3156 percentage points as K increased from 1 to 3, 5, and 8, respectively. Compared with $K = 1$, the $K = 5$ configuration reduced the spectral error by approximately 7.0%. Although $K = 8$ achieved a further reduction in spectral reconstruction error, increasing K from 5 to 8 required processing 60% more historical observations, thereby increasing the input and state-update dimensions. Therefore, $K = 5$ was selected as a practical balance between spectral reconstruction accuracy and computational complexity.

Regarding the correction bound, $c_\Delta = 0.05$ consistently achieved the lowest thickness-state and spectral MAEs across all four historical window lengths under the tested large-error conditions. For $K = 5$, the thickness-state MAE was 1.3184%, representing reductions of approximately 40.7% and 11.9% compared with $c_\Delta = 0.02$ and $c_\Delta = 0.10$, respectively. The corresponding spectral MAE was also the lowest among the three correction bounds, reaching 2.4163 percentage points. Furthermore, the thickness-state MAE decreased from 3.0416% before correction to 1.3184% after correction, corresponding to an improvement of approximately 56.7%. These results demonstrate that $c_\Delta = 0.05$ provides an effective balance between correction magnitude and compensation accuracy, supporting its selection for the proposed monitoring framework.

The finite historical window maintains a fixed state-update dimension throughout the deposition process, enabling efficient local thickness-state correction without expanding the estimation problem as the number of deposited layers increases. To further evaluate the correction of early-layer estimation errors, sequential numerical simulations were performed by introducing initial thickness-state deviations of +3% and +8% at the third layer. For $K = 5$, the corresponding residual estimation errors when this layer exited the active window were 2.773% and 7.773%, respectively. These results illustrate the bounded correction behavior of the finite-window strategy, in which earlier-layer estimates are retained after leaving the active observation window.

To assess the effect of zero-padding during the initial deposition stages, the thickness-state estimation errors were compared between the early padded stages ($N < 5$) and fully populated observation windows ($N \geq 5$). For $K = 5$ and $c_\Delta = 0.05$, the window-averaged MAEs were 1.2207% and 1.3533% under small initial estimation errors, and 1.2804% and 1.3623% under larger initial errors, respectively. At the current-layer level, the corresponding MAEs were 1.1380% and 1.2883% under small initial errors, and 1.2393% and 1.3353% under larger initial errors. Two-sample Kolmogorov–Smirnov tests yielded $p = 0.1150$ and $p = 0.4039$, indicating no statistically significant differences in the overall error distributions at the 5% significance level. Additionally, permutation tests showed a significantly lower early-stage mean error under the small-error condition ($p = 0.0408$), while no significant mean difference was observed under the larger-error condition ($p = 0.2876$). The slightly lower errors during the initial stages may be associated with the relatively simpler optical response of the partially deposited multilayer structure. These results indicate that, despite the reduced number of available historical observations, the validity-mask-assisted zero-padding strategy maintained favorable thickness-estimation accuracy during the initial deposition stages.

3.5. Computational Efficiency Comparison

To quantitatively evaluate the online computational efficiency of the proposed framework, a numerical benchmark was conducted using the same 82-layer coating design and 24 common synthetic test cases. The proposed neural-assisted method was compared with conventional Levenberg–Marquardt (LM) optimization and a random-search-based

optimization baseline. All methods were evaluated using the same initial thickness states, spectral data, and correction constraints. The benchmark was performed in MATLAB R2025b on a workstation equipped with an Intel Core Ultra 7 265KF CPU (3.90 GHz) and 32 GB of RAM. All computations were executed on the CPU without GPU acceleration. Online computation time, thickness-state estimation error, spectral reconstruction error, and forward-model evaluation counts were recorded.

As shown in Table 3, the proposed method achieved a median online CPU inference time of 2.0808 ms per layer, compared with 55.9323 ms for LM optimization and 47.8447 ms for random search, corresponding to computational speedups of approximately 26.9 and 23.0 times, respectively. Furthermore, the proposed method achieved the lowest thickness-state MAE of 1.8322%, compared with 3.9394% and 3.6661% for the two optimization-based methods, while maintaining comparable spectral reconstruction accuracy. Unlike the iterative baselines, which required a median of 752.5 forward-model evaluations, the proposed framework generated thickness-state corrections through direct neural inference. These results demonstrate the substantial reduction in online computational burden achieved by the proposed framework.

Table 3. Comparison of online computational efficiency and reconstruction accuracy among the proposed method, LM optimization, and random search.

Method	Online Time (ms/Layer)	Spectral MAE (pp)	Thickness MAE (%)	TMM Calls
Proposed Method	2.0808	3.1571	1.8322	0
LM Optimization	55.9323	3.0231	3.9394	752.5
Random Search	47.8447	3.0268	3.6661	752.5

Note: Results were obtained from 24 common synthetic test cases using the same 82-layer coating design. Online computation times and TMM evaluation counts are reported as medians, whereas estimation errors are reported as means. Random search was evaluated using three random seeds. The timing excludes offline training, spectral acquisition, and deposition. The proposed method employed $K = 5$ and $c_\Delta = 0.05$.

4. Conclusions

This work presents a neural-assisted triangulation framework for broadband optical monitoring of multilayer optical coatings. By introducing a fixed historical observation window, the framework jointly utilizes residual spectra from multiple recent deposition stages and reformulates the online thickness-estimation step as direct neural prediction of incremental thickness-state corrections. A physics-guided training strategy further constrains the estimated corrections through the corresponding broadband optical response. The proposed framework was implemented on an ion-beam sputtering platform and evaluated through three consecutive fabrication runs of an 82-layer long-wave-pass filter. All three fabricated filters satisfied the specified stopband and passband transmittance requirements. The mean stopband and passband transmittances were 0.112% and 95.057%, respectively, while the cutoff wavelength was 712.461 ± 0.278 nm. These results demonstrate the practical feasibility of the proposed monitoring framework and show limited run-to-run variation in the cutoff position across the three consecutive coating runs. Although the proposed framework uses physics-guided spectral losses to promote consistency with the nominal forward model, it assumes fixed refractive-index profiles during training and online estimation. In practical deposition, variations in film composition and refractive index may introduce model mismatch and affect thickness-state estimation. Incorporating optical-constant uncertainty into the framework will be considered in future work.

Future work will focus on extending the framework to multilayer optical coating systems with increased structural and material complexity, such as structures involving more layers, multiple dielectric material combinations, and stronger material dispersion, while also incorporating additional physical variables, such as incidence angle and polarization,

into the monitoring model. For transition-metal-containing multilayer systems, variations in composition, stoichiometry, or oxidation state may modify the complex refractive index and introduce significant optical absorption. Therefore, for multilayer systems containing strongly absorbing or metallic materials, the present transmittance-based monitoring framework would require further extension to account for absorption and reflection effects.

Author Contributions: Conceptualization, Y.G. and M.J.; methodology, Y.G., X.J. and M.J.; software, Y.G. and X.J.; validation, X.J., M.J., Y.P., B.W. and Z.H.; formal analysis, Y.G., X.J. and M.J.; investigation, X.J., M.J., Y.P., B.W. and Z.H.; resources, M.J., Y.P. and B.W.; data curation, X.J., Y.P., B.W. and Z.H.; writing—original draft preparation, Y.G. and X.J.; writing—review and editing, Y.G., X.J., M.J., Y.P., B.W. and Z.H.; visualization, Y.G. and X.J.; supervision, M.J. and Y.P.; project administration, M.J.; funding acquisition, Y.G. and M.J. All authors have read and agreed to the published version of the manuscript.

Funding: This work was supported in part by the China Postdoctoral Science Foundation under Grant 2024M762771 and Grant GZC20251124, and in part by the Natural Science Basic Research Program in Shaanxi Province of China under Grant 2025JC-YBQN-828.

Institutional Review Board Statement: Not applicable.

Informed Consent Statement: Not applicable.

Data Availability Statement: The data are contained in the manuscript.

Conflicts of Interest: Author Ming Ji, Yuhui Pei, Bo Wang and Zhuangzhuang He were employed by the company IBD Technology Co., Ltd. The remaining authors declare that the research was conducted in the absence of any commercial or financial relationships that could be construed as a potential conflict of interest.

References

1. Ristau, D.; Ehlers, H.; Gross, T.; Lappschies, M. Optical broadband monitoring of conventional and ion processes. *Appl. Opt.* **2006**, *45*, 1495–1501. https://doi.org/10.1364/AO.45.001495.
2. Wilbrandt, S.; Stenzel, O.; Kaiser, N.; Trubetskov, M.K.; Tikhonravov, A.V. In situ optical characterization and reengineering of interference coatings. *Appl. Opt.* **2008**, *47*, C49–C54. https://doi.org/10.1364/AO.47.000C49.
3. Friedrich, K.; Wilbrandt, S.; Stenzel, O.; Kaiser, N.; Hoffmann, K.H. Computational manufacturing of optical interference coatings: Method, simulation results, and comparison with experiment. *Appl. Opt.* **2010**, *49*, 3150–3162. https://doi.org/10.1364/AO.49.003150.
4. Zideluns, J.; Lemarchand, F.; Arhilger, D.; Hagedorn, H.; Lumeau, J. Strategies for in-situ thin film filter monitoring with a broadband spectrometer. *Opt. Express* **2023**, *31*, 9339–9349. https://doi.org/10.1364/OE.484333.
5. Kochikov, I.V.; Sharapova, S.A.; Yagola, A.G.; Tikhonravov, A.V. Correlation of errors in inverse problems of optical coatings monitoring. *J. Inverse Ill-Posed Probl.* **2020**, *28*, 915–921. https://doi.org/10.1515/jiip-2020-0079.
6. Amotchkina, T.V.; Trubetskov, M.K.; Pervak, V.; Schlichting, S.; Ehlers, H.; Ristau, D.; Tikhonravov, A.V. Comparison of algorithms used for optical characterization of multilayer optical coatings. *Appl. Opt.* **2011**, *50*, 3389–3395. https://doi.org/10.1364/AO.50.003389.
7. Isaev, T.F.; Kochikov, I.V.; Lukyanenko, D.V.; Tikhonravov, A.V.; Yagola, A.G. Improving the accuracy of broad-band monitoring of optical coating deposition. *Mosc. Univ. Phys. Bull.* **2018**, *73*, 382–387. https://doi.org/10.3103/S0027134918040070.
8. Tikhonravov, A.; Kochikov, I.; Isaev, T.; Lukyanenko, D.; Yagola, A. Online characterization algorithms for optical coating production with broadband monitoring. *Coatings* **2018**, *8*, 323. https://doi.org/10.3390/coatings8090323.
9. Isaev, T.F.; Kochikov, I.V.; Lukyanenko, D.V.; Tikhonravov, A.V.; Yagola, A.G. Comparison of algorithms for determining the thickness of optical coatings online. *Comput. Math. Math. Phys.* **2019**, *59*, 465–474. https://doi.org/10.1134/S0965542519030102.
10. Melzig, T.; Amochkina, T.; Bruns, S.; Henning, P.; Terhürne, J.; Trubetskov, M.K.; Vergöhl, M. Influence of fitting algorithms on thickness determination during monitoring of optical coatings. *Surf. Coat. Technol.* **2024**, *476*, 130197. https://doi.org/10.1016/j.surfcoat.2023.130197.
11. Tikhonravov, A.V.; Kochikov, I.V.; Yagola, A.G. Error self-compensation mechanism in the optical coating production with direct broad band monitoring. *Opt. Express* **2017**, *25*, 27225–27233. https://doi.org/10.1364/OE.25.027225.
12. Tikhonravov, A.; Kochikov, I.; Matvienko, I.; Isaev, T.; Yagola, A. Strategies of broadband monitoring aimed at minimizing deposition errors. *Coatings* **2019**, *9*, 809. https://doi.org/10.3390/coatings9120809.

13. Tikhonravov, A.V.; Sharov, A.N.; Romanov, B.; Kirpichenko, S.; Sharapova, S.A.; Yagola, A.G. On the selection of broadband monitoring algorithms for optical coating production. *Opt. Express* **2025**, *33*, 16610–16619. https://doi.org/10.1364/OE.559120.
14. Sharov, A.N.; Torbin, S.S.; Lukyanenko, D.V.; Chaikovskii, D.A. Non-local algorithm for broadband monitoring of the optical coating deposition process. *Opt. Contin.* **2026**, *5*, 1678–1688. https://doi.org/10.1364/OPTCON.600314.
15. Lininger, A.; Hinczewski, M.; Strangi, G. General inverse design of layered thin-film materials with convolutional neural networks. *ACS Photonics* **2021**, *8*, 3641–3650. https://doi.org/10.1021/acsphotonics.1c01498.
16. Fan, L.; Chen, A.; Li, T.; Chu, J.; Tang, Y.; Wang, J.; Zhao, M.; Shen, T.; Zheng, M.; Guan, F.; et al. Thin-film neural networks for optical inverse problem. *Light Adv. Manuf.* **2021**, *2*, 395–402. https://doi.org/10.37188/lam.2021.027.
17. Luce, A.; Mahdavi, A.; Wankerl, H.; Marquardt, F. Investigation of inverse design of multilayer thin-films with conditional invertible neural networks. *Mach. Learn. Sci. Technol.* **2023**, *4*, 015014. https://doi.org/10.1088/2632-2153/acb48d.
18. Han, J.H. Efficient inverse design of optical multilayer nano-thin films using neural network principles: Backpropagation and gradient descent. *Nanoscale* **2024**, *16*, 17165–17175. https://doi.org/10.1039/D4NR01667J.
19. Ma, T.; Wang, H.; Guo, L.J. OptoGPT: A foundation model for inverse design in optical multilayer thin film structures. *Opto-Electron. Adv.* **2024**, *7*, 240062. https://doi.org/10.29026/oea.2024.240062.
20. Ma, T.; Ma, M.; Guo, L.J. Optical multilayer thin film structure inverse design: From optimization to deep learning. *iScience* **2025**, *28*, 112222. https://doi.org/10.1016/j.isci.2025.112222.
21. Dai, J.; Ji, X.; Niu, X.; Jiao, H.; Cheng, X.; Wang, Z.; Zhang, J. Transformer neural network-based algorithm for manufacturing error inversion of optical coatings. In *Optica OIC—Optical Interference Coatings Conference 2025, Technical Digest Series*; Optica Publishing Group: Washington, DC, USA, 2025 ; Paper ME.10. https://doi.org/10.1364/OIC.2025.ME.10.
22. Ji, M.; Guo, Y.; Pei, Y.; Qin, Z.; Liu, W.; Hon, C. Research on a broadband optical monitoring method with an improved error compensation mechanism. *Coatings* **2025**, *15*, 551. https://doi.org/10.3390/coatings15050551.
23. Karniadakis, G.E.; Kevrekidis, I.G.; Lu, L.; Perdikaris, P.; Wang, S.; Yang, L. Physics-informed machine learning. *Nat. Rev. Phys.* **2021**, *3*, 422–440. https://doi.org/10.1038/s42254-021-00314-5.
24. Kim, Q.; Lee, S.; Ma, A.; Kim, J.; Noh, H.-K.; Chang, K.B.; Cheon, W.; Yi, S.; Jeong, J.; Kim, B.; et al. A simulation physics-guided neural network for predicting semiconductor structure with few experimental data. *Solid-State Electron.* **2023**, *201*, 108568. https://doi.org/10.1016/j.sse.2022.108568.
25. Yesilyurt, O.; Peana, S.; Mkhitaryan, V.; Pagadala, K.; Shalaev, V.M.; Kildishev, A.V.; Boltasseva, A. Fabrication-conscious neural network based inverse design of single-material variable-index multilayer films. *Nanophotonics* **2023**, *12*, 993–1006. https://doi.org/10.1515/nanoph-2022-0537.

Disclaimer/Publisher's Note: The statements, opinions and data contained in all publications are solely those of the individual author(s) and contributor(s) and not of MDPI and/or the editor(s). MDPI and/or the editor(s) disclaim responsibility for any injury to people or property resulting from any ideas, methods, instructions or products referred to in the content.